EXPRESS LETTER

Ocean-wave phenomenon around Japan due to the 2022 Tonga eruption observed by the wide and dense ocean-bottom pressure gauge networks

Hisahiko Kubo[*], Tatsuya Kubota, Wataru Suzuki, Shin Aoi, Osamu Sandanbata, Naotaka Chikasada and Hideki Ueda

Abstract

Ocean-bottom pressure gauges of wide and dense ocean-bottom observation networks around Japan, S-net and DONET, observed ocean waves caused by the Tonga eruption that started at approximately 13:00 JST (UTC + 0900) on January 15, 2022. We scrutinized the waveform records of the arriving ocean waves to evaluate their nature and found two significant disturbances between 20:00 and 21:00 and after 22:00. The first disturbance with a positive-polarity pulse dominated by long-period components (1000–3000 s) arrived at S-net and DONET stations between 20:00 and 21:00 from the southeast, corresponding to the direction of the short great circle between Tonga and Japan. This arrival was much earlier than expected for a direct tsunami from the volcano and can be explained by assuming that the waves propagated along the short great circle path at a velocity of approximately 300 m/s. After 22:00, significant phases dominated by relatively shorter period components (< 1000 s) arrived from the southeast direction in both observation networks. In DONET, another phase arrived from the south–southeast direction at approximately 23:30 with shorter period components (approximately 500 s). Most of the near-trench S-net stations recorded the peak amplitude during the first disturbance, whereas the near-coast S-net stations and DONET stations observed their peak after 22:00. The amplitudes of ocean-bottom pressure changes in both networks increased as the water depth decreases. This amplification behavior differed between the first and second disturbances, which is attributed to the differences in the natures of the arriving ocean and air waves. This study also found several arrivals of air-wave disturbances to be correlated with the ocean-wave phases, which implies that multiple disturbances of ocean-bottom pressures were generated by the interactions of several disturbances of air waves following the 2022 Tonga eruption with ocean waves.

Keywords: 2022 Tonga eruption, Ocean-bottom pressure disturbances, Ocean-bottom pressure gauge observation around Japan, Relationship with atmospheric pressure disturbances

*Correspondence: hkubo@bosai.go.jp

National Research Institute for Earth Science and Disaster Resilience, 3-1 Tennodai, Tsukuba, Ibaraki 305-0006, Japan

Kubo *et al. Earth, Planets and Space*   (2022) 74:104

Page 2 of 11

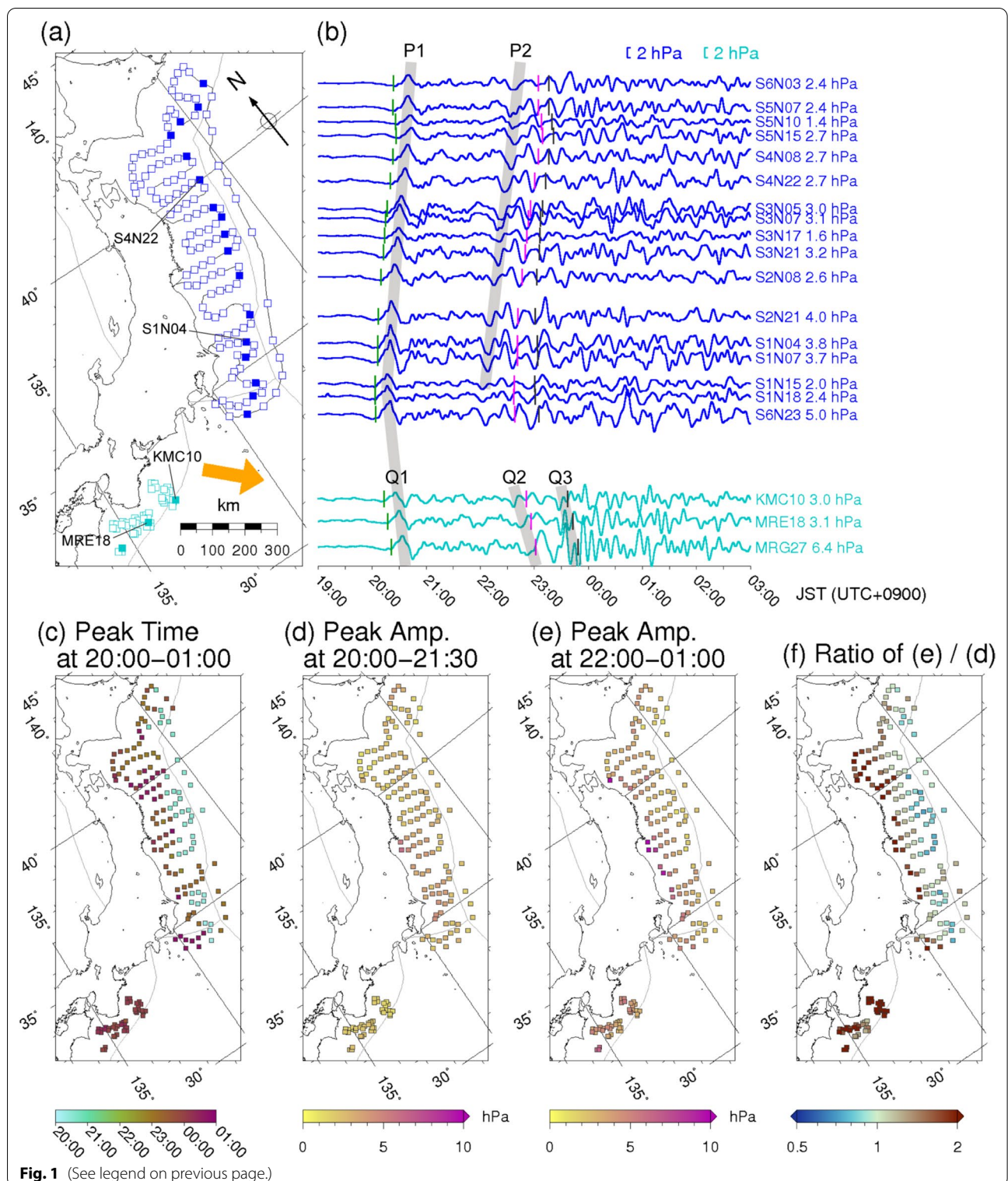## Graphical abstract
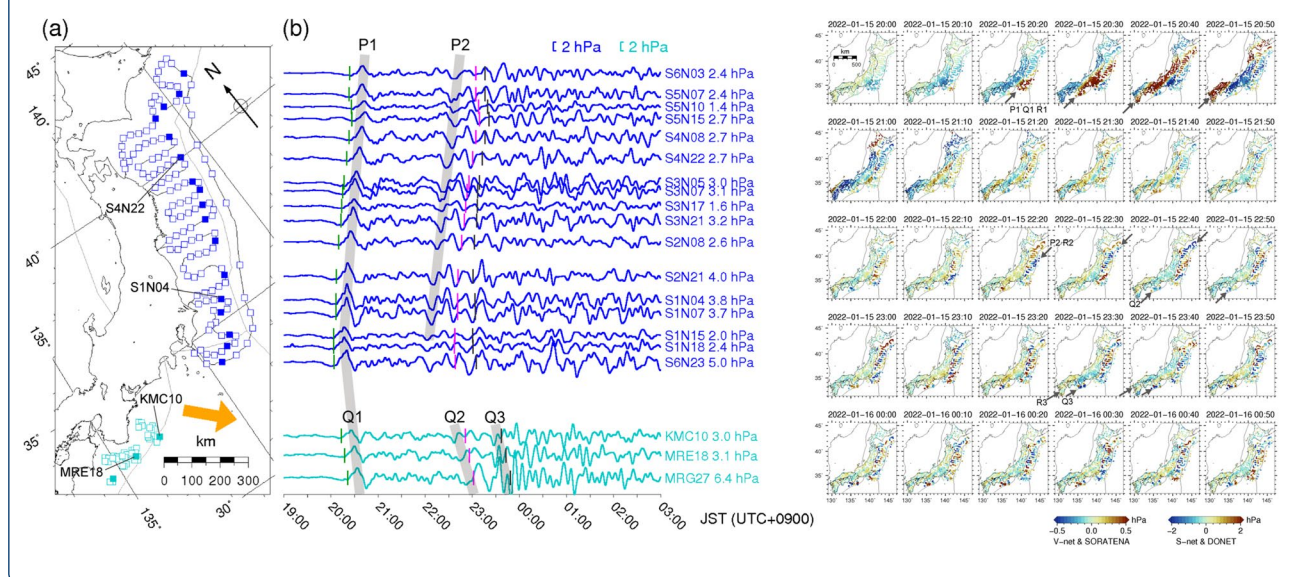
Introduction

At the Hunga Tonga–Hunga Ha'apai volcano (Global Volcanism Program 2013), volcanic activity had increased since late December 2021, and large eruptions occurred on January 14 and 15, 2022. The eruption on January 15 was particularly large accompanied by a powerful explosion, producing a huge plume, atmospheric waves, and ocean waves that traversed the Pacific Ocean (Global Volcanism Program 2022; Gusman and Roger 2022; NOAA Center for Tsunami Research 2022). Sea-level changes caused by the eruption were observed over a wide area around the Pacific Ocean rim and were also reported in other ocean basins, including the Caribbean and Mediterranean seas (NOAA Center for Tsunami Research 2022). In Japan, sea-level changes were observed along the Pacific coastline starting at approximately 20:30, Japan Standard Time (JST) on January 15 (Coordinated Universal Time, UTC+0900). The observed sea-level changes exceeded 1 m in some locations, 1.1 m at Kuji

Port in Iwate Prefecture at 2:26 on January 16, and 1.2 m at Kominato in Amami City, Kagoshima Prefecture at 23:55 on January 15 (JMA 2022).

Along the Pacific Ocean side of Japan, National Research Institute for Earth Science and Disaster Resilience (NIED) has deployed two large-scale ocean-bottom observation networks for earthquake and tsunami (Fig. 1a): S-net, Seafloor observation network for earthquakes and tsunamis along the Japan Trench (Kanazawa et al. 2016; Uehira et al. 2016; Mochizuki et al. 2016; Aoi et al. 2020) is located from Hokkaido to offshore Chiba Prefecture, eastern Japan, and DONET, Dense Ocean-floor Network system for Earthquakes and Tsunamis (Kaneda et al. 2015; Kawaguchi et al. 2015; Aoi et al. 2020) is located in Kumano-nada and off Kii Channel in the Nankai Trough region of western Japan. The ocean-bottom pressure gauges of these systems observed ocean waves caused by the 2022 Tonga eruption. The geodesic distances and azimuths from the stations to the Hunga

(See figure on next page.)
Fig. 1 a Map of the study area. Blue and cyan squares indicate S-net and DONET stations used in this study, respectively. Solid squares denote stations for which waveform records are shown in **b**. The orange arrow indicates a direction that is 140° clockwise from north, which roughly corresponds to the direction of the short great circle between Tonga and Japan. **b** Record section of ocean-bottom pressure from 20:00 JST (UTC + 0900) on January 15, 2022, to 03:00 JST on January 16, 2022. Blue and cyan lines denote waveform records of ocean-bottom pressure gauges at S-net and DONET stations, respectively. Significant phases (P1, P2, Q1, Q2, and Q3) are shaded in gray. Black bars indicate the theoretical arrival times of direct tsunamis. The origin time of the tsunami travel time was assumed at 13:00 (Gusman and Roger 2022). Green and pink bars indicate the theoretical travel times assuming propagation along the short great circle path from the Hunga Tonga–Hunga Ha'apai volcano at velocities of 300 and 220 m/s, respectively. **c** Distribution of peak time of ocean-bottom pressure change between 20:00 and 01:00. **d** Distribution of peak amplitude of ocean-bottom pressure change at 20:00–21:30. **e** Same as **c** but at 22:00–01:00. **f** Distribution of the ratio of **d** the peak amplitude at 20:00–21:30 to **e** the peak amplitude at 22:00–01:00

Kubo *et al. Earth, Planets and Space* (2022) 74:104

Page 3 of 11

Fig. 1 (See legend on previous page.)

Tonga–Hunga Ha'apai volcano are 7600–8100 km and 130°–142°, respectively. In this study, we scrutinized the waveform records of the ocean-bottom pressure gauges

to evaluate the nature of the arriving waves. First, we overviewed the waveform records of the ocean-bottom pressure gauges and detected significant disturbances of

Kubo *et al. Earth, Planets and Space*   (2022) 74:104

Page 4 of 11

ocean-bottom pressure with several distinctive phases. Then, by taking advantage of the high spatial density and the wide coverage of the S-net and DONET stations, we probed the characteristics of the phases by an array analysis and investigate the spatial–temporal distribution of peak amplitude of ocean-bottom pressure. We also examined the relationship between the ocean-bottom pressure disturbances and the atmospheric pressure disturbances to interpret the origins of these ocean waves.

Overview of observed waveforms of ocean-bottom pressure

Figure 1b shows the waveforms recorded by the ocean-bottom pressure gauges at S-net and DONET stations from 19:00 JST on January 15 to 3:00 JST on January 16. Time will henceforth be expressed in JST throughout this study. The waveforms were filtered using a zero-phase Butterworth bandpass filter in the period band of 360 s and 3600 s, and then were resampled at 1 Hz. In most cases of earthquake-induced tsunamis, ocean-bottom pressure changes can be directly converted to sea-surface height changes without considering atmospheric pressure changes. However, the ocean-bottom pressure changes following the 2022 Tonga eruption possibly contain the non-negligible effect of atmospheric pressure changes as well as sea-surface height changes. Hence, we did not convert the ocean-bottom pressure changes to sea-surface height changes.

Two significant disturbances with several distinctive phases were found between 20:00 and 21:00 and after 22:00 (Fig. 1b). The first significant phase arrived at all stations between 20:00 and 21:00. We call this phase P1 at the S-net stations and Q1 at the DONET stations. The more southeasterly the station is, the earlier the first phase was observed. The polarity was positive and the waveforms were similar among S-net and DONET stations. The arrival of the first phase was approximately 3 h earlier than that theoretically expected for tsunamis that generated near the volcano at the time of the eruption (black bars in Fig. 1b). This observed arrival is consistent with the propagation along the short great circle path from the Hunga Tonga–Hunga Ha'apai volcano at a velocity of approximately 300 m/s; in Fig. 1b, green bars indicate the theoretical travel times assuming propagation along the short great circle path at a velocity of 300 m/s. After 22:00, several phases with large amplitudes arrived; however, their behavior differed between S-net and DONET stations. In S-net, a negative-pulse phase (P2 in Fig. 1b) and subsequent phases crossed from south to north after 22:00. In DONET, a relatively large-amplitude phase with negative polarity arrived before 23:00 (Q2 in Fig. 1b), and subsequently, another phase with a large amplitude arrived at approximately 23:30 (Q3

in Fig. 1b). The Q2 phase seemed a little unclear, but was selected based on its relationship with the P2 phase in terms of arrival time and polarity. The dominant period of Q3 was shorter than those of Q1 and Q2. In this study, we focused on these phases and investigated their characteristics by array analysis.

Array analysis in S-net

The wavefield of ocean-bottom pressure in S-net was derived by interpolating the observed data (Fig. 2; see the movie in Additional file 2). Here, the original data were pre-processed using the blockmean command in Generic Mapping Tools (GMT; Wessel and Smith 1998), and the interpolation with continuous curvature splines was conducted using the surface command in GMT. At 20:10–21:00, the P1 phase with a positive pulse crossed from south to north. It propagated toward the northwest (NW) with an almost-linear wavefront. At 22:10–22:40, the P2 phase with a negative pulse propagated toward the NW with an almost-linear wavefront. Subsequently, disturbances with similar wavefronts arrived at several times. After 00:00, waves propagating toward the NW and reflected waves along the coast were observed.

To investigate the direction-of-arrival of the P1 and P2 phases, a semblance analysis (e.g., Neidell and Taner 1971; Honda et al. 2008; Kubota et al. 2021) was performed on arrays consisting of three or more near-trench stations with similar waveforms and water depths. Here, the bandpass-filtered waveforms in the period of 360–3600 s were analyzed with a time window of 1800 s and a sliding interval of 600 s. Assuming a plane-wave incidence, we estimated the velocity and the direction of arrival. Considering the range of water depths at S-net and DONET stations (approximately 2000–7000 m), the search range for the velocity was set between 100 and 340 m/s. Figure 3 shows the results of the semblance analysis at the selected arrays, and the results for all arrays are shown in of Additional file 1: Fig. S1. We found that the direction-of-arrival of P1 at approximately 20:30 was close to southeast (SE) in all arrays. This direction corresponds to that of the short great circle between Tonga and Japan (cyan line in Fig. 3). The direction-of-arrival of P2 at approximately 22:20 was also close to SE. Because of the low resolution in the estimation of velocity, we will not discuss it here; however, it has little effect on the results of the estimation of the direction-of-arrival.

Figure 3 also shows scalograms of ocean-bottom pressure gauge data at two S-net stations, and of Additional file 1: Fig. S1 shows scalograms at other stations. They were derived from continuous wavelet transform of the waveforms using TF-SIGNAL (Kristeková 2006) with the Morlet wavelet as a mother wavelet. The dominant
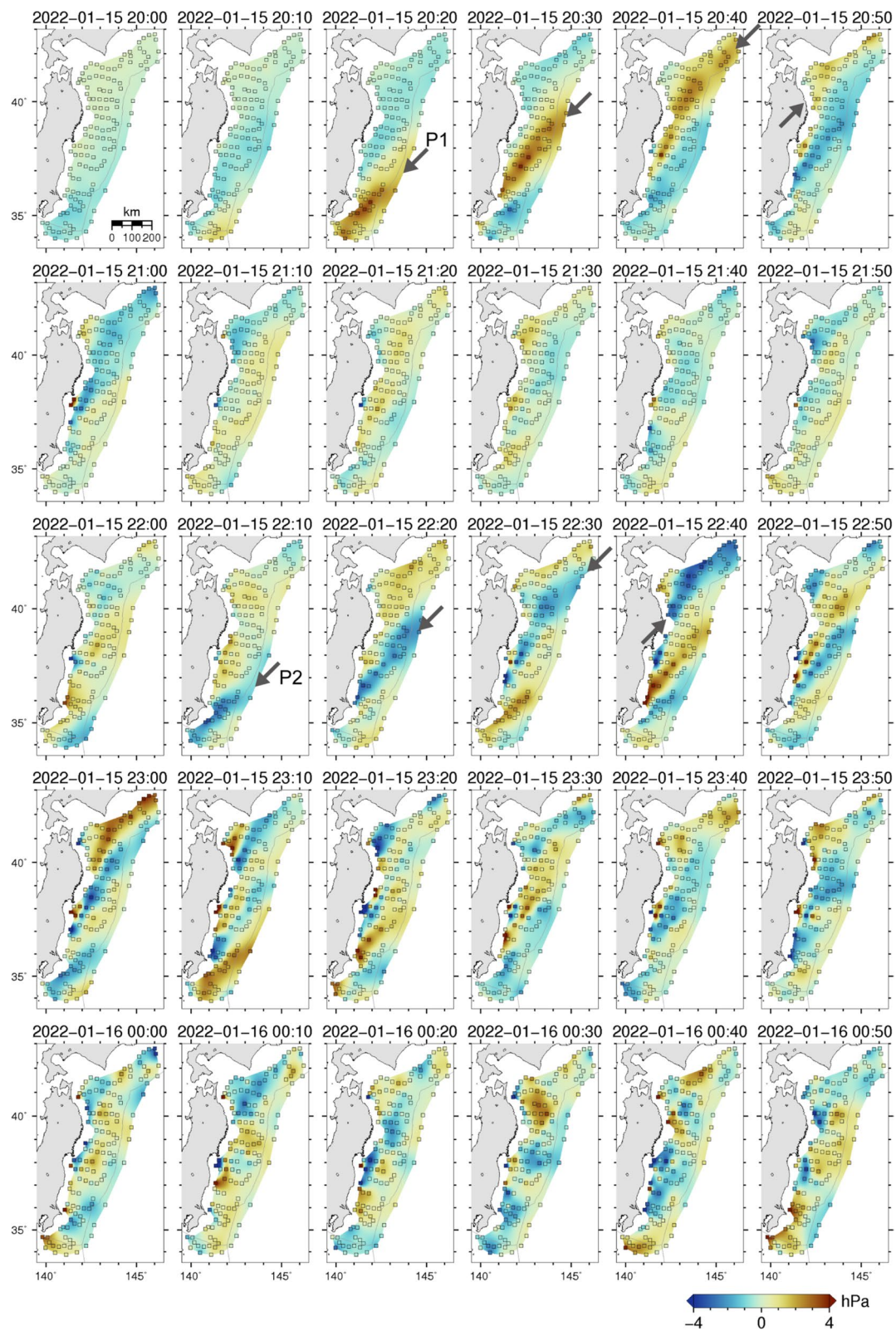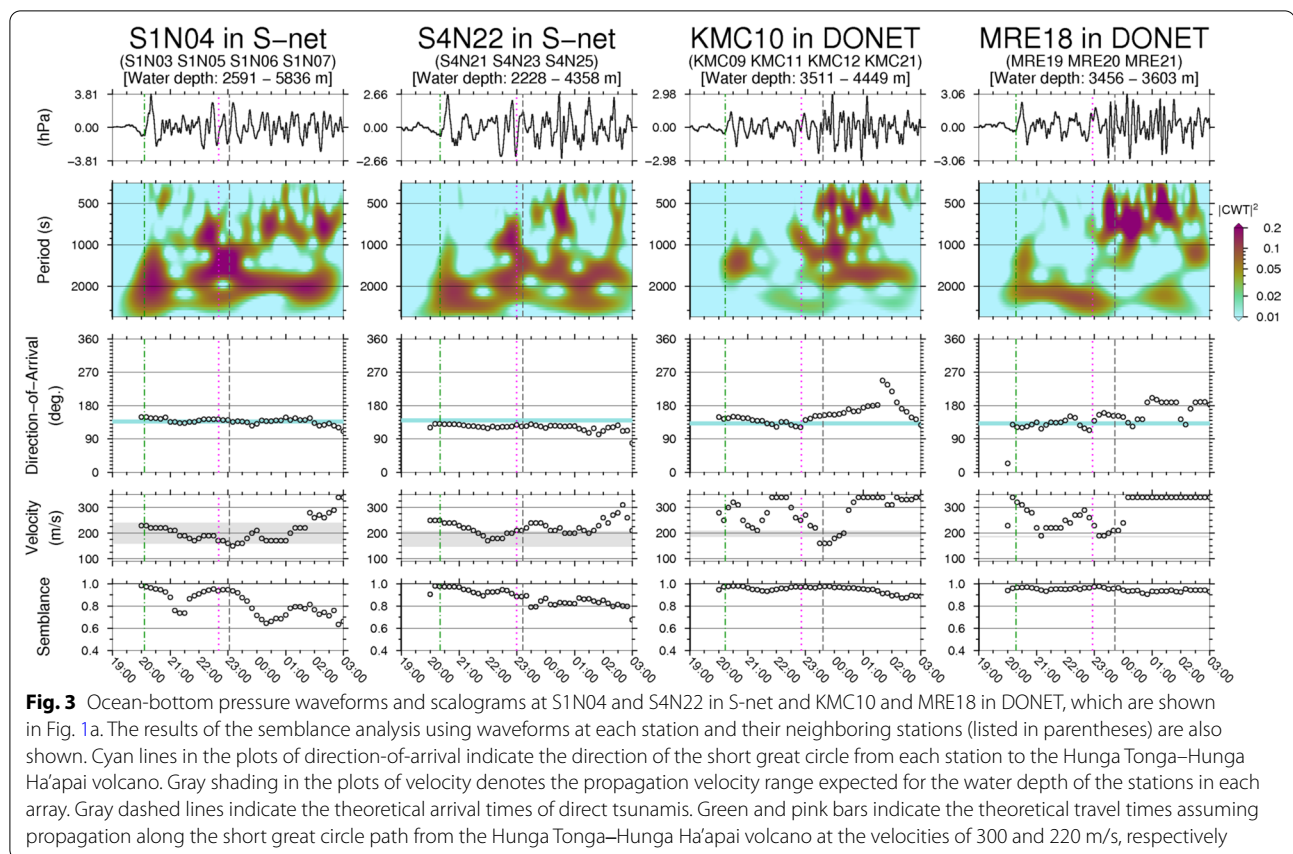
Kubo *et al. Earth, Planets and Space* (2022) 74:104

Page 5 of 11

Fig. 2 Snapshot of the ocean-bottom pressure wavefield derived by interpolating S-net observations. Squares indicate S-net observation stations

Kubo *et al. Earth, Planets and Space* (2022) 74:104

Page 6 of 11

Fig. 3 Ocean-bottom pressure waveforms and scalograms at S1N04 and S4N22 in S-net and KMC10 and MRE18 in DONET, which are shown in Fig. 1a. The results of the semblance analysis using waveforms at each station and their neighboring stations (listed in parentheses) are also shown. Cyan lines in the plots of direction-of-arrival indicate the direction of the short great circle from each station to the Hunga Tonga–Hunga Ha'apai volcano. Gray shading in the plots of velocity denotes the propagation velocity range expected for the water depth of the stations in each array. Gray dashed lines indicate the theoretical arrival times of direct tsunamis. Green and pink bars indicate the theoretical travel times assuming propagation along the short great circle path from the Hunga Tonga–Hunga Ha'apai volcano at the velocities of 300 and 220 m/s, respectively

period components differed between P1 and P2; long-period components (1000–3000 s) were dominant in P1, while short-period components (< 1000 s) were more prevalent in P2 and subsequent phases. This difference in the dominant period was also observed in the wavefield of S-net (Fig. 2); the wavelength of P1 was longer than those of P2 and subsequent phases.
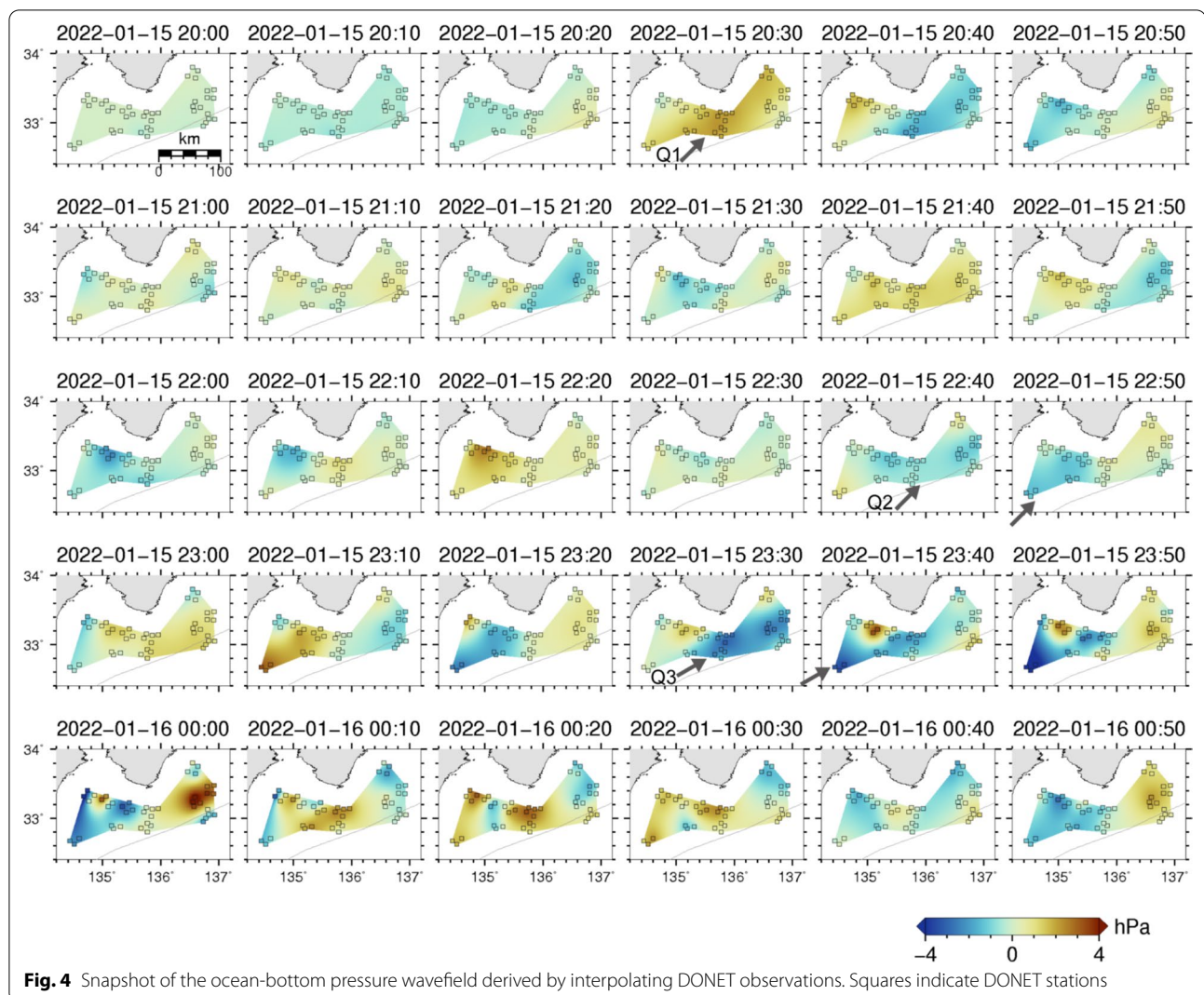
Additional file 1: Fig. S2 shows the waveform trace of ocean-bottom pressure from the near-trench stations to the near-coast stations. At near-trench stations, such as S6N12 and S3N19, the arrival of the first phase was consistent with the assumption of a propagation velocity of 300 m/s. However, the first phase at near-coast stations such as S3N12 and S3N13 arrived slightly after the theoretical arrival time for a propagation velocity of 300 m/s. This indicates that the wave propagation velocity decreased with the decrease in the water depth, which was also observed in subsequent phases. Because of this difference in wave propagation velocity with depth, the wavefronts of P1 and P2 shown in Fig. 2 rotated counterclockwise as they propagated across the observation network. Additional file 1: Fig. S2 also indicates that the sharpness of the first phase is lower at the near-coast stations than that at the near-trench stations.

Array analysis in DONET

We investigated the significant phases Q1, Q2, and Q3 at DONET stations. Figure 4 shows the wavefield of ocean-bottom pressure in DONET (see the movie in Additional file 3). At approximately 20:30, the first phase Q1 with a positive pulse propagated toward the NW. Before 23:00, the Q2 phase propagated toward the NW. Then, another phase Q3 arrived with a significantly large amplitude at approximately 23:30. After 00:00, the wavefield in DONET became complex likely because of the coastal reflection effect.

Array analysis shown in and Fig. 3 and Additional file 1: Fig. S1 suggests that the directions of arrival of Q1 and Q2 were close to SE at all DONET arrays, which corresponds to the direction of the short great circle between Tonga and Japan. The Q3 phase arrived from the south–southeast (SSE) direction, which is slightly off the direction of the short great circle path from the Tonga volcano. This difference in the direction-of-arrival is also found in the wavefield of ocean-bottom pressure (Fig. 4); the wavefront of Q3 rotated clockwise compared with those of Q1 and Q2.

The scalograms for DONET stations (Fig. 3, Additional file 1: Fig. S2) clearly indicate differences in the

Kubo *et al. Earth, Planets and Space*   (2022) 74:104

Page 7 of 11

Fig. 4 Snapshot of the ocean-bottom pressure wavefield derived by interpolating DONET observations. Squares indicate DONET stations

dominant period components among the three phases. Long-period components (1000–3000 s) were dominant in Q1, while the components of the period band between 700 and 1000 s were dominant in Q2 and short-period components (approximately 500 s) were dominant in Q3.

Distributions of peak amplitude and peak time

The peak time of ocean-bottom pressure varied among the station locations (Fig. 1c). Most of the near-trench S-net stations recorded a peak at 20:00–21:00 corresponding to the first disturbance, whereas the near-coast S-net stations and DONET stations observed their peak during the second disturbance after 22:00. Figure 1d, e shows the spatial distribution of peak amplitude for the first and second disturbances, respectively. The amplitudes of ocean-bottom pressure change increased with the decrease in the water depth

in both disturbances. During the first disturbance, P1 and Q1, the observed amplitudes were 1–2 hPa at most stations, while some near-coast S-net stations observed amplitudes of 4–5 hPa. The amplitudes between 22:00 and 01:00 at the near-trench S-net stations were comparable to those of the first disturbance, while the near-coast S-net stations observed larger amplitudes during this period, with a maximum of over 10 hPa. DONET stations observed the largest amplitudes (3–5 hPa) during the Q3 and subsequent phases, which were larger than those of the first disturbance (1–2 hPa).

The amplitude ratio between the first and second disturbances differed between the near-trench and near-coast S-net stations (Fig. 1f), which indicates that the amplification of ocean-bottom water pressure in response to a decrease in water depth differed between the first and second disturbances. This difference may

Kubo *et al. Earth, Planets and Space*   (2022) 74:104

Page 8 of 11

have been caused by differences in the dominant period (wavelength) of the arriving waves, differences in the degree of coupling of air and ocean waves, and differences in the direct contribution of atmospheric pressure changes to ocean-bottom pressure changes.

Relationship with atmospheric pressure disturbance

Following the 2022 Tonga eruption, ocean waves and atmospheric waves were observed worldwide, and their correlation has been highlighted (Global Volcanism Program 2022; Kubota et al. 2022). Following the Krakatoa eruption in 1883, correlated disturbances in tide gauge and atmospheric pressure were also observed (Symons 1888; Ewing and Press 1955), which were expected to have been caused by the coupling of ocean and air waves (Press and Harkrider 1966; Harkrider and Press 1967; Garrett 1970; Francis 1985). Here, to interpret the origin of the observed ocean waves around Japan following the 2022 Tonga eruption, we jointly investigated ocean-bottom pressure and atmospheric pressure data.

The spatial and temporal distributions of ocean-bottom pressure and atmospheric pressure are shown in Fig. 5 (see the movie in Additional file 4). For the atmospheric pressure data, we used records of micro barometers of the Fundamental Volcano Observation Network, V-net of NIED (Tanada et al. 2017; Aoi et al. 2020), which were installed at active volcanoes in Japan, and atmospheric pressure records from proprietary weather sensors, Soratena, of Weathernews Inc. (Weathernews Inc. 2022). The waveforms of atmospheric pressure were filtered using a zero-phase Butterworth bandpass filter in the period band of 360 s and 3600 s, as well as those of ocean-bottom pressure. At approximately 20:30, the first disturbance of atmospheric pressure R1 propagated toward the NW with an almost-linear wavefront, which correlated with the first disturbance of ocean-bottom pressure P1 and Q1. Additional file 1: Fig. S3 shows the waveform trace of ocean-bottom pressure at the S-net and DONET stations and atmospheric pressure at the V-net stations along the geodesic distance from the Hunga Tonga–Hunga Ha'apai volcano. A positive pulse at V-net stations (R1) arrived at 20:00–21:00, whose arrival time and waveform were consistent with those of the first pulse at S-net and DONET stations (P1 and Q1). The arrival of R1 was consistent with the propagation along the short great circle path from the Hunga Tonga–Hunga Ha'apai volcano at a velocity of approximately 300 m/s, as well as P1 and Q1. The first atmospheric disturbance R1 was expected to be Lamb waves, an acoustic mode of air waves with a propagation velocity of approximately 300 m/s (Lamb 1932; Nishida et al. 2014). Kubota et al. (2022) clarified through a global simulation that the

atmospheric pressure disturbance due to Lamb waves generated by the 2022 Tonga eruption forcibly induced the sea-surface uplift and that a superposition of the atmospheric pressure change by the Lamb waves and induced sea-surface change was observed by ocean-bottom pressure gauges as ocean-bottom pressure. This can explain the similar waveform and arrival time in the first disturbance of atmospheric pressure and ocean-bottom pressure. The peak amplitude of atmospheric pressure during the first disturbance was approximately 1 hPa at the V-net stations, while those of ocean-bottom pressure were approximately 1–2 hPa at the near-trench ocean-bottom stations. The amplitude difference between the ocean-bottom and atmospheric pressure changes is expected to correspond to the sea-surface height changes of uplift forcibly induced by Lamb waves. The arrival delay of the first phase and the decrease in its sharpness at near-coast stations (Additional file 1: Fig. S2) imply that the couplings between Lamb waves and induced ocean waves began to break at shallow water depths, which was pointed out by Tanioka et al. (2022).

At approximately 22:30, another atmospheric pressure disturbance R2 propagating along the NW was observed, which correlated with the observed ocean-bottom pressure changes P2 and Q2. At approximately 23:30, DONET observed another phase arriving from the SSE direction (Q3 in Fig. 5). At around the same time, an atmospheric pressure disturbance arrived from the SSE direction with an almost-linear wavefront (R3 in Fig. 5). Kubota et al. (2022) suggested that after the arrival of ocean waves due to Lamb waves, ocean gravity waves arrived with the propagation velocity of tsunamis (approximately 200–220 m/s) for most parts of the Pacific Ocean in which the water depth is approximately 4000–5000 m. Their expected arrival time (pink bars in Fig. 1b, Additional file 1: Fig. S3) roughly corresponded to the arrival time of the second synchronous disturbance of atmospheric pressure and ocean-bottom pressure. The ocean gravity waves originated from various factors such as subsidence ocean waves compensating for the uplift by Lamb waves, ocean waves displaced by atmospheric gravity waves and their resonances, tsunamis directly caused by eruption-induced crustal deformation near the volcano, and waves induced by topographic effects, such as scattered waves. Atmospheric gravity waves, a type of atmospheric wave (Harkrider and Press 1967), were excited by the volcanic eruption. Some components of the atmospheric gravity waves, such as higher modes GR_1 or GR_2 (Harkrider and Press 1967), have a propagation velocity close to that of tsunamis, especially at periods shorter than 1000 s because of the dispersion of higher modes of atmospheric gravity waves. Owing to the resonance effect between the atmospheric waves and the ocean waves, in which their
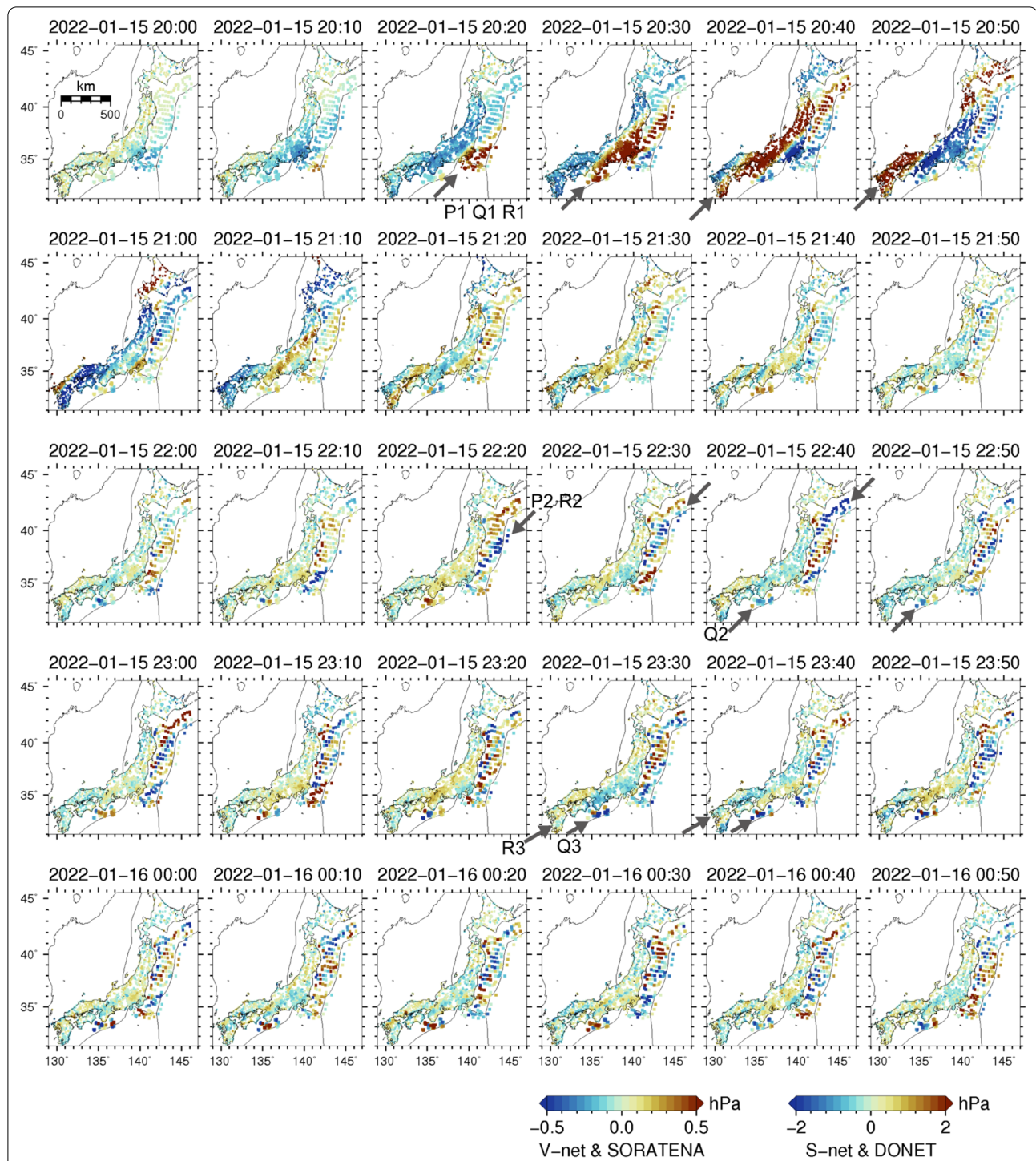
Kubo *et al. Earth, Planets and Space*   (2022) 74:104

Page 9 of 11

Fig. 5 Spatial and temporal distributions of ocean-bottom pressure and atmospheric pressure. Circles indicate V-net and SORATENA observations, while squares denote S-net and DONET observations. Different color pallets are used for the ocean-bottom pressure and atmospheric pressure data

propagation velocities are close to each other (Proudman 1929), the amplitude of ocean-bottom water pressure disturbance caused by atmospheric gravity waves increases with the propagation distance r at a rate of $\sim r^{1/2}$ (Kubota et al. 2022). This study presents that relatively shorter period components (< 1000 s) were dominant in the P2,

Kubo *et al. Earth, Planets and Space*   (2022) 74:104

Page 10 of 11

Q2, and subsequent phases, which supports the occurrence of the resonance effect between the atmospheric gravity waves and ocean waves. Meanwhile, the amplitudes of ocean waves due to Lamb waves and tsunamis caused by crustal deformation and scattering decrease at a rate of $\sim r^{-1/2}$ because of the geometrical spreading effect. As shown in Additional file 1: Fig. S3, the amplitude of atmospheric pressure after 22:00 (< 0.2 hPa) was much lower than that of the first disturbance, while the amplitude of the ocean-bottom pressure after 22:00 was comparable to or larger than that of the first disturbance. This indicates that the direct contribution of atmospheric pressure changes to ocean-bottom pressure changes was insignificant after 22:00. Therefore, it is likely that the ocean-bottom pressure change after 22:00 consisted mainly of ocean gravity waves caused by atmospheric gravity waves, although further analysis is required.

Notably, the ocean-bottom pressure disturbance of Q3 came from a different direction than the short great circle direction from the Hunga Tonga–Hunga Ha'apai volcano. The arrival of the atmospheric pressure disturbance of R3 from a similar direction at approximately the same time implies a relationship between Q3 and R3. Therefore, further research should be conducted using global simulations of air and ocean waves with a realistic global meteorological model.

Abbreviations

DONET: Dense oceanfloor network system for earthquakes and tsunamis; GMT: Generic mapping tools; JMA: Japan meteorological agency; JST: Japan standard time; NIED: National research institute for earth science and disaster resilience; NOAA: National oceanic and atmospheric administration; NW: Northwest; SE: Southeast; S-net: Seafloor observation network for earthquakes and tsunamis along the Japan Trench; SSE: South–southeast; UTC: Coordinated universal time; V-net: The fundamental volcano observation network.

Supplementary Information

The online version contains supplementary material available at https://doi.org/10.1186/s40623-022-01663-w.

Additional file 1. Ocean-bottom pressure waveforms and scalograms including the results of semblance analysis for 16 arrays, waveform trace of ocean-bottom pressure from near-trench S-net stations to near-coast S-net stations, and waveform trace of atmospheric pressure and ocean-bottom pressure along the geodesic distance from the Hunga Tonga–Hunga Ha'apai volcano.

Additional file 2. Movie of the wavefield of ocean-bottom pressure in S-net associated with Fig. 2.

Additional file 3. Movie of the wavefield of ocean-bottom pressure in DONET associated with Fig. 4.

Additional file 4. Movie of the spatial and temporal distributions of ocean-bottom pressure and atmospheric pressure around Japan associated with Fig. 5.

Declarations

Ethics approval and consent to participate
Not applicable.

Consent for publication
Not applicable.

Competing interests
The authors have no competing interests to declare.

References

Aoi S, Asano Y, Kunugi T, Kimura T, Uehira K, Takahashi N, Ueda H, Shiomi K, Matsumoto T, Fujiwara H (2020) MOWLAS: NIED observation network for earthquake, tsunami and volcano. Earth, Planet Space 72:126. https://doi.org/10.1186/s40623-020-01250-x

Ewing M, Press F (1955) Tide-gage disturbances from the great eruption of Krakatoa. Trans Am Gephys Union 36:53–60. https://doi.org/10.1029/TR036i001p00053

Francis PW (1985) The origin of the 1883 Krakatau tsunamis. J Volcanol Geotherm Res 25:349–363. https://doi.org/10.1016/0377-0273(85)90021-6

Garrett JR (1970) A theory of the Krakatoa tide gauge disturbances. Tellus 22(1):43–52. https://doi.org/10.3402/tellusa.v22i1.10157

Global Volcanism Program (2013) Hunga Tonga-Hunga Ha'apai (243040) in Volcanoes of the World, v. 4.10.6 (24 Mar 2022). Venzke, E (ed.). Smithsonian Institution. https://volcano.si.edu/volcano.cfm?vn=243040. Accessed 6 May 2022

Global Volcanism Program (2022) Report on Hunga Tonga-Hunga Ha'apai (Tonga). In: Sennert SK (ed) Weekly Volcanic Activity Report, 12 January–18 January 2022. Smithsonian Institution and US Geological Survey. https://volcano.si.edu/showreport.cfm?doi=GVP.WVAR20220112-243040. Accessed 6 May 2022

Gusman AR, Roger J (2022) Hunga Tonga - Hunga Ha'apai volcano-induced sea level oscillations and tsunami simulations. https://doi.org/10.21420/DYKJ-RK41 Accessed 6 May 2022

Kubo *et al. Earth, Planets and Space*   (2022) 74:104

Page 11 of 11

Harkrider D, Press F (1967) The Krakatoa air-sea waves: an example of pulse propagation in coupled system. Geophys J Int 13(1–3):149–159. https://doi.org/10.1111/j.1365-246X.1967.tb02150.x

Honda R, Aoi S, Sekiguchi H, Fujiwara H (2008) Imaging an asperity of the 2003 Tokachi-oki earthquake using a dense strong-motion seismograph network. Geophys J Int 172:1104–1116. https://doi.org/10.1111/j.1365-246X.2007.03702.x

JMA (2022) Tidal level change due to the large eruption of Hunga Tonga–Hunga Ha'apai volcano near the Tonga Islands at 13:00 on January 15, 2022 (2nd Report). https://www.jma.go.jp/jma/press/2201/16b/202201161415.html. Accessed 6 May 2022

Kanazawa T, Uehira K, Mochizuki M, Shinbo T, Fujimoto H, Noguchi S, Kunugi T, Shiomi K, Aoi S, Matsumoto T, Sekiguchi S, Okada Y (2016) S-net project, cabled observation network for earthquakes and tsunamis. SubOptic WE2B-3.

Kaneda Y, Kawaguchi K, Araki E, Matsumoto H, Nakamura T, Kamiya S, Ariyoshi K, Hori T, Baba T, Takahashi N (2015) Development and application of an advanced ocean floor network system for megathrust earthquakes and tsunamis. Seafloor Observ. https://doi.org/10.1007/978-3-642-11374-1_25

Kawaguchi K, Kaneko S, Nishida T, Komine T (2015) Construction of the DONET real-time seafloor observatory for earthquakes and tsunami monitoring. Seafloor Observ. https://doi.org/10.1007/978-3-642-11374-1_10

Kristeková M (2006) Time-frequency analysis of seismic signals. Ph.D. Thesis, Geophysical Institute, Slovak Academy of Sciences, Bratislava, Slovakia.

Kubota T, Saito T, Chikasada NY, Sandanbata O (2021) Meteotsunami observed by the deep-ocean seafloor pressure gauge network off northeastern Japan. Geophys Res Lett 48:e2021GL094255. https://doi.org/10.1029/2021GL094255

Kubota T, Saito T, Nishida K (2022) Global fast-traveling tsunamis driven by atmospheric Lamb waves on the 2022 Tonga eruption. Science. https://doi.org/10.1126/science.abo4364

Lamb H (1932) Hydrodynamics. Dover, Mineola

Mochizuki M, Kanazawa T, Uehira K, Shimbo T, Shiomi K, Kunugi T, Aoi S, Matsumoto T, Sekiguchi S, Yamamoto N, Takahashi N, Shinohara M, Yamada T (2016) S-net project: Construction of large scale seafloor observatory network for tsunamis and earthquakes in Japan. AGU Fall Meeting, NH43B–1840.

Neidell NS, Taner MT (1971) Semblance and other coherency measures for multichannel data. Geophysics 36:482–497. https://doi.org/10.1190/1.1440186

NIED (2019a) NIED V-net. NIED. https://doi.org/10.17598/nied.0006

NIED (2019b) NIED S-net. NIED. https://doi.org/10.17598/nied.0007

NIED (2019c) NIED DONET. NIED. https://doi.org/10.17598/nied.0008

NIED (2022a) Ocean bottom pressure data recorded by NIED S-net after Hunga Tonga - Hunga Ha'apai volcano eruption. NIED. https://doi.org/10.17598/NIED.0007-2022-001

NIED (2022b) Ocean bottom pressure data recorded by NIED DONET after Hunga Tonga - Hunga Ha'apai volcano eruption. NIED. https://doi.org/10.17598/NIED.0008-2022-001

Nishida K, Kobayashi N, Fukao Y (2014) Background lamb waves in the earth's atmosphere. Geophys J Int 196:312–316. https://doi.org/10.1093/gji/ggt413

NOAA Center for Tsunami Research (2022) Hunga Tonga-Hunga Ha'apai Volcano-generated Tsunami. https://nctr.pmel.noaa.gov/tonga20220115/ Accessed 6 May 2022

Press F, Harkrider D (1966) Air-sea waves from the explosion of Krakatoa. Science 154(3754):1325–1327. https://doi.org/10.1126/science.154.3754.1325

Proudman J (1929) The Effects on the sea of changes in atmospheric pressure. Geophys Suppl Mon Notices Royal Astron Soc 2(4):197–209. https://doi.org/10.1111/j.1365-246X.1929.tb05408.x

Symons G (1888) The eruption of Krakatoa and subsequent phenomena. Quart J Roy Meteor Soc 14:301–307. https://doi.org/10.1002/qj.4970146809

Tanada T, Ueda H, Nagai M, Ukawa M (2017) NIED's V-net, the fundamental volcano observation network in Japan. J Disaster Res 12(5):926–931. https://doi.org/10.20965/jdr.2017.p0926

Tanioka Y, Yamanaka Y, Nakagaki T (2022) Characteristics of tsunamis observed in Japan due to the air wave from the 2022 Tonga eruption. Earth Planet Space 74:61. https://doi.org/10.1186/s40623-022-01614-5

Uehira K, Kanazawa T, Mochizuki M, Fujimoto H, Noguchi S, Shinbo T, Shiomi K, Kunugi T, Aoi S, Matsumoto T, Sekiguchi S, Okada Y, Shinohara M, Yamada T (2016) Outline of seafloor observation network for earthquakes and tsunamis along the Japan Trench (S-net) EGU General Assembly 2016, EGU2016–13832

Weathernews Inc. (2022) Atmospheric pressure data from soratena weather sensors offered to researchers free of charge. https://global.weathernews.com/wp-content/uploads/2022/01/20220128_1.pdf

Wessel P, Smith WHF (1998) New, improved version of generic mapping tools released. EOS Trans Am Geophys Un 79:579

Publisher's Note

Springer Nature remains neutral with regard to jurisdictional claims in published maps and institutional affiliations.